# Molecular Chemistry-Controlled Hybrid Ink-Derived Efficient Cu$_2$ZnSnS$_4$ Photocathodes for Photoelectrochemical Water Splitting

Wooseok Yang,[†] Yunjung Oh,[†] Jimin Kim,[†] Myung Jin Jeong,[‡] Jong Hyeok Park,[‡] and Jooho Moon*,[†]

[†]Department of Materials Science and Engineering and [‡]Department of Chemical and Biomolecular Engineering, Yonsei University, 50 Yonsei-ro, Seodaemun-gu, Seoul 120-749, Republic of Korea

S *Supporting Information*

ABSTRACT: To realize economically competitive hydrogen production through photoelectrochemical (PEC) water splitting, it is essential to develop an efficient photoelectrode consisting of earth-abundant constituents in conjunction with low-cost solution processing. Cu$_2$ZnSnS$_4$ (CZTS) has received significant attention as a promising photocathode owing to its abundance and good absorption properties. However, the efficiency of the solution-processed CZTS photocathode is not yet comparable to its counterparts. Here, a hybrid ink, obtained by careful control of precursor mixing order, was used to produce a highly efficient CZTS photocathode. The molecular chemistry-controlled hybrid ink formulation, particularly the roles of thiourea−Sn^{2+} complexation, was elucidated by liquid Raman spectroscopy. The hybrid ink-derived CZTS thin films modified with conformal coating of an n-type TiO$_2$/CdS double layer and a Pt electrocatalyst achieved an exceptionally high photocurrent of 13 mA cm^{-2} at −0.2 V versus a reversible hydrogen electrode under 1 sun illumination. The modified photocathodes showed relatively stable H$_2$ production with faradaic efficiency close to unity.
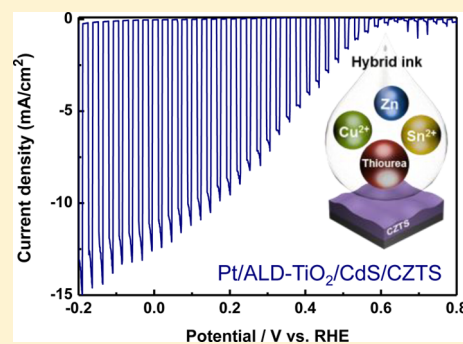
Realization of a sustainable energy economy is contingent on developing technology that enables the conversion of renewable resources into an energy vector suitable for storage, transportation, and consumption. In the recently released *Hydrogen and Fuel Cells Technology Roadmap* from the International Energy Agency, hydrogen is highlighted as an attractive energy carrier for this purpose, as it can utilize the current infrastructure for fossil fuels that is already in place.[1] Moreover, hydrogen is advantageous for facilitating significant reductions in energy-related CO$_2$ emissions with its low-carbon footprint. Semiconductor-based photoelectrochemical (PEC) water splitting is the one of the most promising technologies for generating hydrogen by harnessing the enormous amount of renewable energy delivered from the Sun to the Earth, in conjunction with photovoltaic coupled electrolysis and photocatalytic water splitting. Since the first observation of PEC water splitting by Fujishima and Honda,[2] many research groups have sought to boost the solar-to-hydrogen (STH) conversion efficiency while ensuring cost-competitiveness. STH efficiencies >20% may be necessary for commercialization. On the basis of a recent calculation by the Lewis group,[3] the maximum STH efficiency of 29.7% can be achieved using a dual absorber (D4-type) PEC tandem cell composed of a series-connected n-type photoanode and a p-type photocathode, which is the most efficient configuration for PEC water splitting. Extensive investigations have been carried out to obtain promising

photoanode materials to explore diverse n-type semiconductors with a high photocurrent and stability. In contrast, only a few studies have been reported for p-type photocathodes for PEC water splitting. While Huang et al. reported a survey of the recent efforts in developing photocathodes for hydrogen production,[4] it is still a challenge to obtain p-type semiconductors using low-cost materials and processes with high performance.

Among the various options available for p-type photocathode PEC water splitting, p-Cu$_2$O is an attractive candidate because of its appreciable performance and abundancy.[5−8] However, p-Cu$_2$O has poor stability in aqueous solutions because the redox potentials for monovalent copper oxide lie between the valence and conduction bands of Cu$_2$O. This instability makes the hermetic thin protective layer indispensable, thereby raising the device complexity and manufacturing cost. At the same time, p-type chalcogenide materials such as p-CuIn$_x$Ga$_{(1-x)}$Se$_2$ (CIGSe), p-CuInS$_2$, p-CuGaSe$_2$, and p-Cu$_2$ZnSnS$_4$ (CZTS) have also received increasing interest.[9−11] In particular, nontoxicity and abundance of CZTS make it a promising material for low-cost and large-scale PEC devices. In this regard, a coevaporated Pt/TiO$_2$/CdS/CZTS photocathode was demonstrated, revealing a
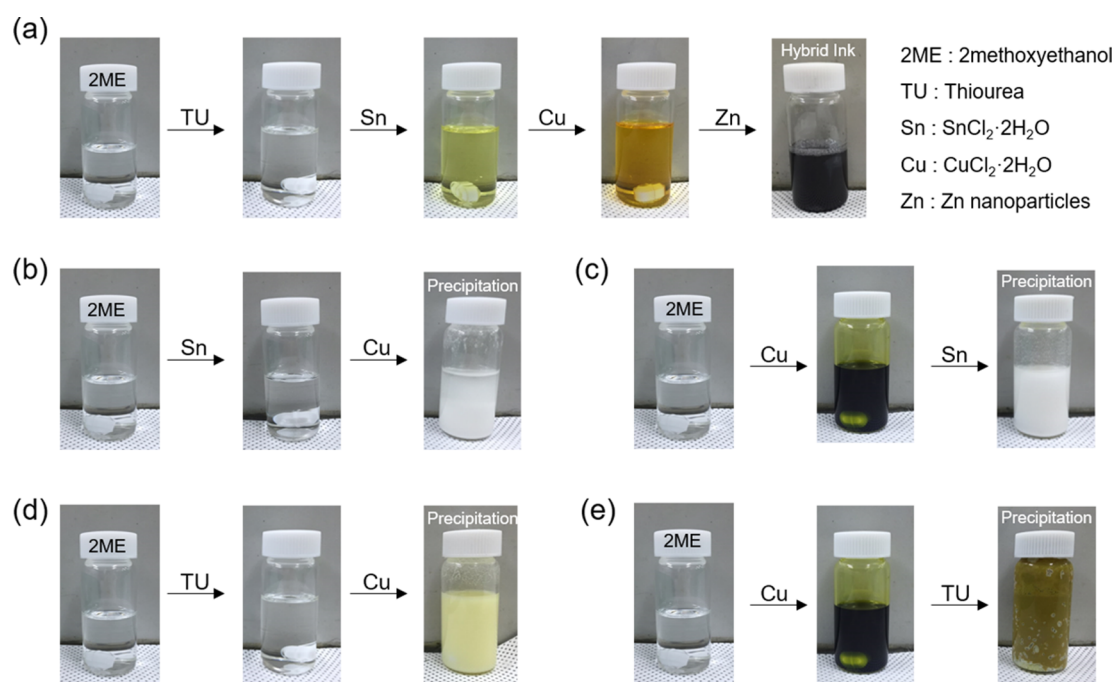
Figure 1. Photographs of (a) the desirable route for synthesizing the homogeneous CZTS hybrid ink containing ionic TU−Sn−Cu complexes with well-dispersed metallic Zn nanoparticles. (b, c) The absence of the TU complexing agent results in precipitation, and (d, e) undesirable mixing orders of the precursors also produce the precipitate.

high photocurrent density near the 8 mA cm^{-2} level.[12] More scalable routes like sol−gel spin-coating, electrodeposition, doctor blading, and the electrophoretic deposition of nano-crystal ink have also been reported as alternatives to expensive vacuum-based deposition processes.[13−16] However, the effi-ciencies of solution-processed CZTS photocathodes are substantially low, presumably because of the phase impurity and low crystallinity of solution-derived CZTS thin films. Recently, relatively efficient photocathodes based on electro-deposited CZTS were reported by Jiang et al., exhibiting a photocurrent density of 9.3 mA cm^{-2} at 0 V versus a reversible hydrogen electrode (vs RHE).[17] However, they focused on a simple demonstration of the PEC performance without a systematic study of the relationship between processing conditions and phase formation and lacked an in-depth analysis of CZTS precursor inks.

The all-soluble precursor route is generally vulnerable to contamination from impurities such as carbon and oxygen because of incomplete decomposition of soluble precursors. This inevitably involves significant shrinkage and leads to the formation of porous structures with a small grain size.[18] In contrast, the CZTS nanocrystal dispersion method offers stoichiometric advantages and purity controls at a molecular scale. However, it is difficult to fabricate dense organic residue-free thick films from the dispersion of nanocrystals capped with stabilizing molecules using complex nanoparticle synthesis.[19] A slurry approach, in which all insoluble precursor particles are suspended in alcohol, also suffers from the difficulty of achieving a homogeneous dispersion of the multicomponent precursor particles.[20] The hydrazine-based hybrid ink approach is the most promising route for fabricating high-quality CZTS thin films because hydrazine is a carbon- and oxygen-free solvent medium in which metal chalcogenides could be dissolved.[21,22] In hydrazine-based hybrid methodologies, S, Se, and metal chalcogenides such as Cu$_2$S and SnSe are

dissolved with no additives, whereas ZnS remains as a particulate species.[23] Despite the unique chemistry of the hydrazine-based approach enabling the fabrication of highly pure and precisely stoichiometry-controlled CZTS films, hydrazine is highly toxic and explosive for practical use. In contrast, we used a nontoxic hybrid ink-based approach to produce high-quality CZTS thin films.[24] Our nontoxic hybrid ink consisted of dissolved ionic Cu and Sn species and thiourea in the presence of a homogeneously dispersed metallic Zn nanopowder in 2-methoxyethanol. However, our previous study simply demonstrated a comparison between Zn and ZnS particles as a Zn source in terms of phase formation and solar cell efficiencies without consideration of the molecular chemistry in hybrid ink formulation. Understanding the molecular chemistry in synthesizing the precursor solution is crucial because the compositional homogeneity in the as-deposited precursor film is dependent upon the chemical interaction among the constituent species. During the annealing process (generally under a H$_2$S atmosphere at 550−580 °C), the detrimental secondary phases can be generated because of the nonuniformity of the as-deposited films and/or the differences in the diffusion rates and reactivities among the metallic species. For example, a high diffusion rate for Cu and the affinity of Cu to react with sulfur led to the formation of copper sulfides on the surface and voids left by the Cu atoms. A significant Sn loss could occur by the evaporation of SnS$_2$ because of its volatile nature; thus, the preferential formation of SnS$_2$ should be avoided.[25] It is also desirable for Zn to occur in the metallic phase because Zn ionic species can more easily form a stable ZnS secondary phase that could slow the CZTS phase transformation.[24] To prevent the elemental loss and detrimental secondary phase while achieving a nontoxic solvent-based homogeneous hybrid ink, a clear understanding of the complexation reactions among Cu, Sn,
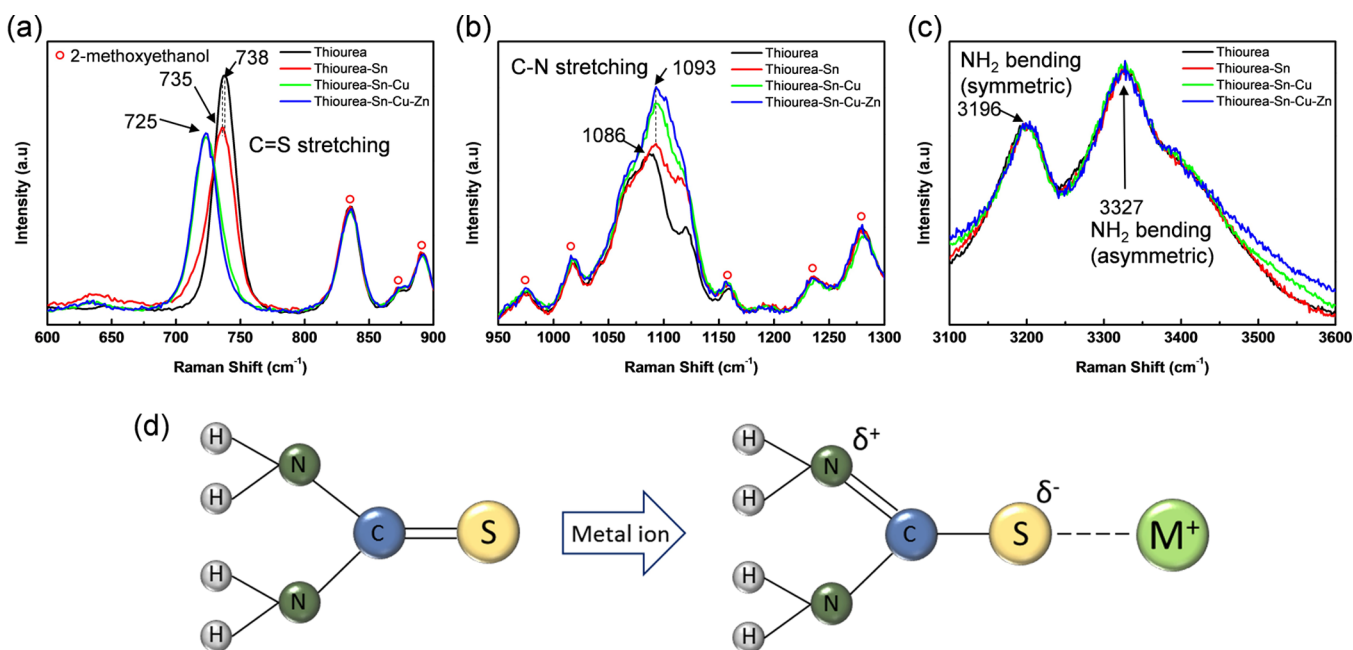
Figure 2. Raman spectra corresponding to (a) C=S stretching, (b) C−N stretching, and (c) NH$_2$ bending for CZTS hybrid inks with sequential addition of each precursor. (d) Schematics of the molecular structure of thiourea before and after bonding with the metal cations.

and sulfur precursors prior to the addition of well-dispersed Zn nanoparticles is necessary.

Thiourea, which is a versatile metal-ion complexing agent, has been extensively used as both a sulfur source and a stabilizer to ensure the dissolution of metal components for the nontoxic CZTS precursor solution.[16,18,26] The synthesis procedure for the solution containing thiourea and the metal cation should be carefully controlled, otherwise the interaction between thiourea and the metal cation occasionally leads to precipitation, which causes inhomogeneity in the solution. However, the interaction between thiourea and the metal components has not yet been elucidated. Here, the role of thiourea in synthesizing the homogeneous solution was investigated by liquid Raman analysis. This is the first study to reveal the interaction between thiourea and a metal cation in solution for CZTS fabrication by liquid Raman spectroscopy. On the basis of a clear understanding of the molecular-level interaction between the precursors, we successfully fabricated compositionally homogeneous and phase-pure CZTS thin films from the synthesized hybrid ink. The subsequent deposition of CdS and TiO$_2$ on CZTS as well as surface decoration with Pt enabled us to demonstrate an unprecedentedly enhanced performance, reaching a record-high performance for a CZTS-based photocathode in terms of a high photocurrent density and onset potential.

A hybrid CZTS ink was synthesized by sequentially dissolving thiourea (TU), tin, and copper precursors in 2-methoxyethanol (2ME), followed by planetary milling with metallic Zn nanoparticles, as shown in Figure 1a. First, TU was mixed with 2ME, resulting in a colorless clear solution. Upon the addition of SnCl$_2$·2H$_2$O to the solution containing TU, the colorless solution gradually changed to a light yellow solution. However, only the SnCl$_2$·2H$_2$O-dissolved solution was colorless (Figure 1b), implying that the TU−Sn complex formation induced the coloration of the solution. Adding CuCl$_2$·2H$_2$O to the TU-Sn solution resulted in a further color change from light to dark yellow without any precipitation. In contrast, Figure

1b−e shows that different mixing orders for the precursors produced a precipitate. Without TU, the white precipitate was generated by mixing SnCl$_2$·2H$_2$O and CuCl$_2$·2H$_2$O, regardless of the mixing order (Figure 1b,c). Adding CuCl$_2$·2H$_2$O into the TU-containing 2ME solution also resulted in an insoluble precipitate and vice versa (Figure 1d,e). This experimental observation implies that the mixing order of the precursors is an important factor, and the complexation reaction between TU and Sn especially plays a critical role in the preparation of the homogeneous Cu−Sn−TU precursor solution without any significant segregation. A hybrid CZTS ink preparation was completed by adding Zn nanoparticles to the clear solution containing TU, Sn, and Cu species, followed by planetary milling for 3 h. A small amount of dispersing additive (BYK 2163) was added to the TU−Sn−Cu solution prior to adding the Zn nanoparticles to ensure a homogeneous dispersion. The dispersed heavy Zn nanoparticles settled slowly under the influence of gravitational forces but returned to an initial well-dispersed state by simple agitation, implying that the dispersing agent successfully prevented the agglomeration of Zn nanoparticles.

Liquid Raman analysis was performed to elucidate the role of the TU−Sn complex. The symmetric stretching vibration of C=S in TU (at 738 cm^{-1}) was slightly shifted to lower wavenumber (735 cm^{-1}) upon the addition of the Sn precursor (Figure 2a), whereas the C−N stretching vibration (Figure 2b) shifted in the opposite direction (from 1086 to 1093 cm^{-1}). The NH$_2$ bending modes (at 3196 and 3327 cm^{-1}) exhibited negligible changes upon the addition of the metal precursors (Figure 2c), indicating a negligible influence of the TU−metal complexation on the bonding character of the hydrogen atoms in TU. For thiourea−metal complexation, two possible coordinations, either through bonding to the nitrogen or through bonding to the sulfur of TU, have been reported.[27,28] The molecular structure of the TU molecule is shown in Figure 2d. The interaction between the metal ions and sulfur in TU is expected to induce an enhanced delocalization of the lone pair
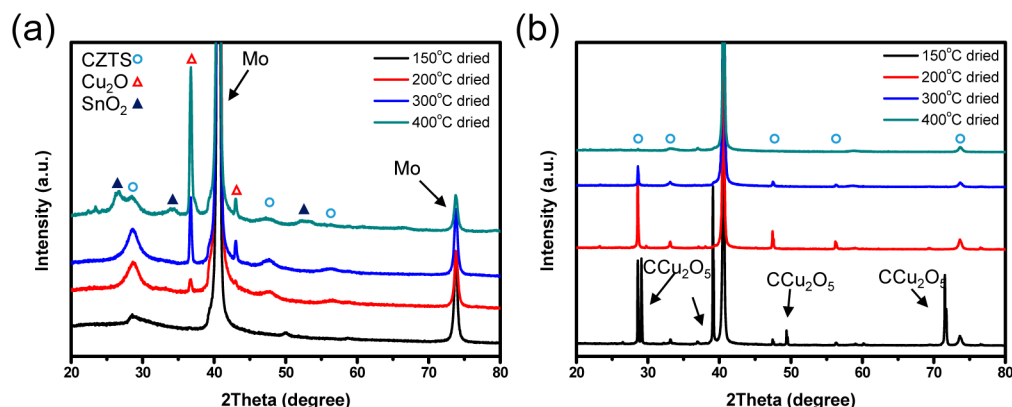
Figure 3. XRD patterns of the (a) as-dried and (b) after sulfurized hybrid ink-derived CZTS films as a function of drying temperatures ranging from 150 to 400 °C. The sulfurization conditions were fixed at 560 °C under a H₂S atmosphere for 30 min.

electrons, resulting in a higher electron density developed on the sulfur atom. The enhanced delocalization reduces the double bonding character of the carbon–sulfur bond, eventually leading to a shift toward negative wavenumbers for the C=S stretching mode, with a positive shift of the C–N stretching mode.[29] Thus, the negative shift after the addition of Sn into the TU-containing solution implies the formation of a TU–Sn complex through the interaction between the Sn^{2+} ion and S in TU. Adding the Cu precursor into the TU–Sn solution largely shifts the C=S vibration to lower wavenumbers (at 725 cm^{-1}), implying the interaction between TU and Cu is stronger than that between TU and Sn (Figure 2a).

To completely formulate the CZTS hybrid ink, metallic Zn nanoparticles were added to the homogeneous TU–Sn–Cu solution by a planetary milling process. The Raman spectrum of the complete CZTS ink (i.e., the TU–Sn–Cu–Zn ink) was almost identical to that of the TU–Sn–Cu ink, suggesting that the Zn metal particles had no effect on the interaction between TU and the metal cations because of the insoluble solid phase. To confirm the state of metallic Zn particles in the hybrid ink, thermogravimetric and differential scanning calorimetry (TG/DSC) analyses were performed under an inert atmosphere for the hybrid ink, which was dried at 250 °C under an inert atmosphere (Figure S1). A strong endothermic peak at ~420 °C is indicative of Zn melting. This explains that the Zn nanoparticles existed in a dispersed metallic state without interacting with the TU–Sn–Cu complexes. In the case of the TU solution containing a Cu precursor without any Sn ions (Figure 1d), which led to a precipitate, the C=S stretching mode appeared at the same position as the TU–Sn–Cu solution, indicating that the interaction between TU and Cu is the same for both solutions (Figure S2). However, there was an additional peak in the TU solution containing the Cu precursor at 667 cm^{-1}, which could be attributed to the polymerization of the TU–Cu complex. Several studies attributed the additional peaks near 640–670 cm^{-1} to polymerization, such as metal–oxygen–metal bridges in a prepared gel formed during the polycondensation process.[30] This additional peak was used as an indicator for the degree of polymerization because the Raman signal was enhanced by the formation of long-range order or periodicity.

The Raman results provide a glimpse as to the importance of the precursor mixing order to prepare the homogeneous CZTS solution. Because Cu^{2+} strongly reacts with S in TU, adding Cu^{2+} ions directly into the TU-containing 2ME solution produces a significant precipitation by the polymerization of

Cu^{2+}–TU. Sn^{2+} ions also react with S in TU, but the interaction between Sn^{2+} and TU is weaker than that between Cu^{2+} and TU, as expressed by the smaller shift of the C=S vibration. The TU–Sn^{2+} complex possibly plays a role in hindering the polymerization of the Cu–TU complex. The TU–Sn–Cu ink needs to be prepared according to the proper mixing order of the precursors to ensure no premature precipitation, after which Zn metallic nanoparticles are well dispersed in the CZTS hybrid ink. This is the first observation of the role of the TU–Sn^{2+} complex in the synthesis of a homogeneous hybrid precursor solution for CZTS thin films.

We fabricated CZTS thin films using our synthesized hybrid inks with the sequential steps of spin coating, air drying, and sulfurization under a H₂S atmosphere. In our previous study on the fabrication of a CZTS nanorod array, the drying temperature strongly affected the phase purity and PEC performance by ensuring both sufficient decomposition of the metal–TU complexes and removal of carbon impurities without too much oxidation and elemental losses.[31] We also performed phase and compositional analyses on the hybrid ink-derived CZTS thin films after sulfurization at 560 °C for 30 min, with different drying temperatures of 150, 200, 300, and 400 °C in air. Note that the effect of the sulfurization conditions had been investigated in our previous study[24] of CZTS thin-film solar cells. Figure 3 shows the X-ray diffraction (XRD) peaks before/after sulfurization as a function of the drying temperatures. For the as-dried over 200 °C samples (Figure 3a), broad CZTS peaks were observed at 28.5°, 47.3°, and 56.1°, reflecting the (112), (220), and (312) planes of kesterite CZTS (JCPDS 26-0575), respectively. No clear peaks were observed in the sample dried at 150 °C, except for the Mo substrate because insufficient decomposition of the TU–metal complexes impeded the formation of metal oxide or metal sulfide compounds. With the increasing drying temperatures, the peaks for binary oxides such as Cu₂O and SnO₂ appeared with broad CZTS peaks. For the sulfurized sample dried at 150 °C, carbon-related impurity peaks were observed because the unremoved carbon during the low-temperature drying process likely reacted with other components during the high-temperature sulfurization process. When the samples were dried at 200 °C, only the CZTS peaks were visible after sulfurization, but the intensities of the CZTS peaks diminished on increasing the drying temperatures above 200 °C. The XRD data indicate that the formation of binary oxides during the air-drying of the precursor films hindered CZTS crystallization during the sulfurization process. A compositional analysis for

the sulfurized CZTS thin films was performed by energy dispersive X-ray spectroscopy (EDS) analysis, as shown in Figure S3. When the drying temperatures were increased, the S/(Cu+Zn+Sn) ratio and the measured deviation increased. This result suggests that significant metal cation losses and nonuniformity were induced by raising the air-drying temperature. In contrast, the carbon concentration decreased as the drying temperature increased. The EDS analysis revealed that the optimum air drying temperature was 200 °C, at which the sample had a Cu-poor and Zn-rich composition (Cu/(Zn+Sn) = 0.91, Zn/Sn = 1.4, S/(Cu+Zn+Sn) = 1.0). As shown in Figure S4, our CZTS thin film contained densely packed and well-grown crystallites with grain sizes above 500 nm. The film thickness was about 1 μm, which was close to that of the other efficient CZTS photocathodes.

To clarify the presence of the secondary phases in our CZTS thin film dried at 200 °C, Raman analysis was performed with two different excitation wavelengths (532 and 325 nm). In both cases, the excitation power was kept below 50 μW to avoid thermal effects during the acquisition of the spectra. With the 532 nm wavelength (Figure S5a), the CZTS film exhibited a strong peak at 337 cm^{-1} with weak shoulder peaks at 287 and 375 cm^{-1}, all of which are attributed to CZTS. There were no noticeable peaks assigned to the secondary phases of the binary or ternary sulfide such as Cu_2SnS_3, Cu_2S, and ZnS. It is noteworthy that the ZnS secondary phase is usually indiscernible from CZTS because the main peak locations for both are similar and the sensitivity of ZnS at 532 nm is low. A very small amount of ZnS ($E_g \sim 3.7$ eV) can be detected using ultraviolet Raman (325 nm wavelength, $E \sim 3.8$ eV) because the intensity of the Raman scattering is greatly enhanced when the incident laser frequency is close in energy to an electronic transition of the compound.[32] In the Raman spectra recorded at 325 nm (Figure S5b), a strong ZnS peak near 347 cm^{-1} was observed with a relatively broad full width at half-maximum (fwhm), implying that the main peak can be deconvoluted into CZTS and ZnS peaks. The relative intensity difference for the CZTS and ZnS peaks did not explain the quantitative comparison between CZTS and ZnS because the resonance Raman signal for ZnS was much higher than that for the normal Raman signal for CZTS. These Raman results indicate the minimal presence of the ZnS secondary phase, but its quantitative amount is still in question. The ZnS secondary phase is considered as an inevitable consequence in the Cu-poor and Zn-rich composition, which is a common feature of even highly efficient CZTS solar cells, to develop shallow acceptors (V_{Cu}) and suppress deep acceptors (Cu_{Zn}).[33] As Berg et al. demonstrated, the detection limits for the secondary phase in CZTS using XRD and Raman spectroscopy were too low; a further analysis tool is necessary to quantitatively discriminate the ZnS impurity from CZTS.[34]

Figure S6 shows the photocurrent density–potential curves of the bare CZTS thin films dried at different temperatures after sulfurization at 560 °C for 30 min. Samples were submerged in 0.5 M Na_2SO_4 aqueous solution (the pH was adjusted to 10 by the addition of NaOH) under simulated light illumination. All samples provided a cathodic photocurrent, indicative of the p-type semiconducting properties of our CZTS thin films. The CZTS film dried at 200 °C showed the largest photocurrent: 166 μA cm^{-2} at −0.2 V vs RHE, which matches well to the phase and composition analysis results. The surface of the p-type photocathodes is commonly coated with thin layers of the n-type buffer layer to form a p−n junction. The

resulting built-in potential, created across the p−n junction by equilibration of the Fermi level, induces a steeper band bending and widens the depletion width, facilitating the charge separation and shifting the onset potential.[35] We deposited an n-type CdS layer using a chemical bath deposition (CBD) process followed by spin-coating a solution-processed TiO_2 layer (s-TiO_2). Pt has a very low overpotential for hydrogen evolution and was also deposited as an electrocatalyst on the n-type layer.

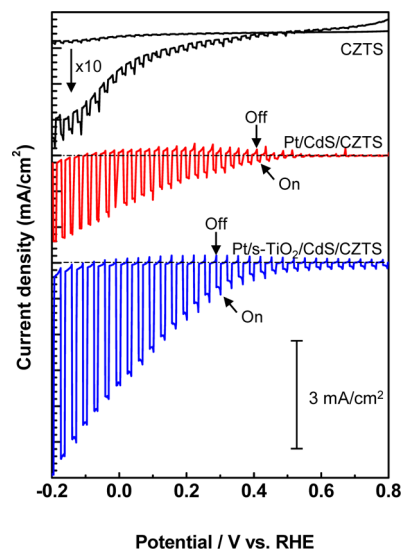Figure 4 shows the PEC properties of the CZTS photocathode with the deposition of n-type layers and the Pt catalyst

Figure 4. Current density−potential curves of the CZTS, Pt/CdS/CZTS, and Pt/s-TiO$_2$/CdS/CZTS photocathodes in a 0.5 M Na$_2$SO$_4$ aqueous solution (pH adjusted to 10 by the addition of NaOH) under chopped solar-simulated light illumination (AM 1.5G). The s-TiO$_2$ layer was deposited by an ethanol-based solution process. The scan rate was 5 mV/s with a negative scan direction.

under the same measurement conditions used for Figure S6. A significant enhancement of the photocurrent was achieved by the deposition of a CdS layer, as expected from the results for similar systems.[12,17] The thickness of CdS was optimized by controlling the CBD times, as shown in Figure S7. The influence of the CdS thickness on the p-type chalcopyrite thin films has been discussed elsewhere.[11] The photocurrent density at −0.2 V vs RHE of the Pt/CdS/CZTS electrode reached 2.2 mA cm^{-2}, which is over 13 times higher than that of the CZTS electrode. It is noteworthy that no distinct enhancement in the photocurrent was observed despite the high catalytic property of Pt catalyst (Figure S8). This observation suggests that the main limitation of the CZTS photocathode relates to slow charge separation rather than low catalytic activity as discussed in the literature.[36] Using a s-TiO$_2$/CdS double n-type layer, further enhancement of the photocurrent density was observed: the photocurrent density above 5.5 mA cm^{-2} at −0.2 V vs RHE. In addition to improved photocurrent, a shift of the onset potential was also observed upon deposition of n-TiO$_2$ layer. It is noteworthy that flat band potential can be estimated from the onset potential where a photocurrent arises.[13] We define the onset potentials as the potential showing 50 μA cm^{-2} of cathodic photocurrent in the $I−E$ curves according to the literature.[37] In a recent study of the efficient CZTS-based photocathode in the optimum Pt/In$_2$S$_3$/CdS/CZTS structure,

the onset potentials of both Pt/In$_2$S$_3$/CdS/CZTS (0.63 V vs RHE) electrode and Pt/CdS/CZTS (0.64 V vs RHE) were nearly identical (i.e., the n-type In$_2$S$_3$ layer did not affect the onset potential despite the photocurrent improvement).[17] In our case, the insertion of the n-TiO$_2$ layer resulted in a significant shift of the onset potential to 0.86 V vs RHE compared to the Pt/CdS/CZTS electrode (0.53 V vs RHE). This result suggests that TiO$_2$ was more efficient than In$_2$S$_3$, probably because the band gap of TiO$_2$ ($\sim$3.2 eV) is greater than that of In$_2$S$_3$ ($\sim$2.24 eV). The deeper valence band of TiO$_2$ is believed to induce a larger electrostatic repulsion of holes from the surface, thereby reducing surface recombinations.[35] It should be noted that the determination of onset potential for a bare CZTS sample would yield an arbitrary value because of high off-current level, indicating that the onset simply represents the decomposition potential. The large onset potential, implying large flat band potential, for our Pt/s-TiO$_2$/CdS/CZTS photocathode is a record value for a CZTS-based photoelectrode, which is beneficial for developing zero-bias tandem cells. The schematic band diagram depicting the energetics of the Pt/TiO$_2$/CdS/CZTS photocathode before and after equilibrium in the electrolyte is presented in Figure S9. The flat band potentials of CZTS, CdS, and TiO$_2$ are assumed to be 0.65, $-$0.1, and $-$0.2 V vs RHE, respectively.[35,38] The Fermi level and band alignment among CZTS, CdS, and TiO$_2$ were reported in the literature.[35,39] In a schematic diagram, the equilibration would lead to form a type-II heterojunction where the electrons can selectively transfer from CZTS to the electrolyte through the multijunction of CdS and TiO$_2$. In contrast, the deposition of TiO$_2$ directly on the CZTS film would result in deactivation of photoelectrochemical properties of CZTS because the interface between CZTS and TiO$_2$ would act as a recombination center possibly because of large band gap difference, as discussed in the literature.[38]

To further boost the photocurrent of our hybrid ink-derived CZTS-based electrode, the PEC performance was evaluated in an aqueous mixed solution of 0.5 M Na$_2$SO$_4$, 0.25 M Na$_2$HPO$_4$, and 0.25 M NaH$_2$PO$_4$ (the pH was adjusted to 6.85 by NaOH addition) under simulated AM 1.5 G irradiation (Figure 5a). The photocurrent of the Pt/s-TiO$_2$/CdS/CZTS electrode reached a remarkably high value of 21.5 mA cm^{-2} at $-$0.2 V vs RHE. It is worth noting the presence of higher transient current spike at larger cathodic bias. The transient current spike results from the recombination of photogenerated carrier due to two possible origins. First, interfacial trap states and/or sluggish charge transfer kinetics can cause recombination, so that the photocurrent spike is likely to disappear at larger cathodic bias. Second, the recombination due to the reduced species of the redox couple at the electrode/electrolyte interface can result in the transient current spike preferred at higher photocurrent region. In our case, the presence of photocurrent spike can be attributed to drastic consumption of redox couple at higher cathodic bias.[13] Kumagai et al. elucidated the difference between the Na$_2$SO$_4$ and phosphate buffer solutions by obtaining current−potential curves of a rotating Pt disk electrode in both solutions. Through the Pt electrochemistry, they ascribed the origin of the difference to the variations in the hydrogen evolution reaction (HER) at the surface of the Pt particles and/or the role of the buffer species that stabilize the pH in the vicinity of the electrode surface, which reduces the chemical bias, thus promoting the HER.[9] Our results of the comparison between two electrolytes are in good agreement with the previous study on the Pt/CdS/CIGSe
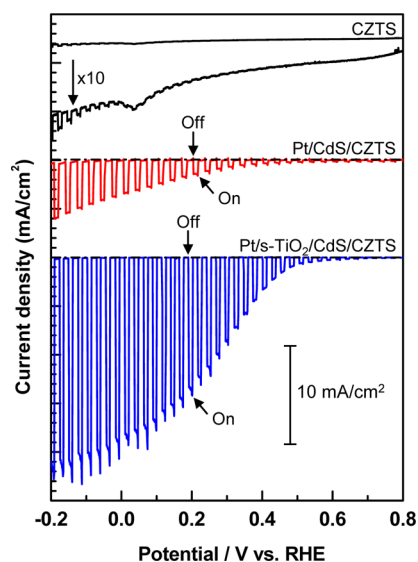

Figure 5. Current density−potential curves of the CZTS, Pt/CdS/CZTS, and Pt/s-TiO$_2$/CdS/CZTS photocathodes in a phosphate-buffered aqueous solution with pH 6.85 under chopped solar-simulated light illumination (AM 1.5G). The scan rate was 5 mV/s with a negative scan direction.

photocathodes and the theory of near-surface ion distribution and buffer effect.[9,40] The amount of evolved H$_2$ from the Pt/s-TiO$_2$/CdS/CZTS photocathode was evaluated in the three-electrode configuration at 0 V vs RHE under AM 1.5G radiation by gas chromatography (GC). Figure S10 shows the typical time course curves for both H$_2$ evolution from the photocathode with an active area of 0.16 cm^2 and one-half of the electrons passing through the outer circuit (e^-/2) as expressed by a solid line. When the determined hydrogen generation is compared with the expected amount calculated by the photocurrent, the faradaic efficiency (i.e., the ratio of the rate of H$_2$ evolution to that of e^-/2) can be calculated. Despite the exceptionally high photocurrent, the solution-processed TiO$_2$-based photocathode reveals 45−55% of faradaic efficiency, indicating the presence of side reactions rather than H$_2$ evolution, possibly due to an incomplete coverage of thin TiO$_2$.

Device stability is one of the most crucial features to realize commercially viable water splitting. Because CZTS and CdS are relatively unstable during the PEC measurement compared to TiO$_2$, a conformally coated TiO$_2$ layer is necessary to achieve stable PEC performance. The spin-coating process for the TiO$_2$ layer was optimized based on linear sweep voltammograms and chronoamperometric measurements at 0 V vs RHE (Figure S11). Despite the high photocurrent with a relatively thin TiO$_2$ layer (single or double coating of 0.05 M TiO$_2$ precursor solution), the photocurrent remained at only 15% of its initial value after 1 h. This instability presumably resulted from the incomplete coverage of the thin TiO$_2$ layer on the CdS/CZTS surfaces. Although the relatively thick spin-coated TiO$_2$ layer (double coating of a 0.1 M TiO$_2$ solution) on the CZTS-based photocathode yielded a better stability (retained 55% of its initial value after 1 h), the photocurrent level was substantially diminished compared to the thin TiO$_2$ layer, likely because of the charge recombination and optical loss associated with a thick TiO$_2$ layer.

To achieve a better stable photocathode with a high photocurrent, we used atomic layer deposition (ALD) for the TiO$_2$ layer, which is a desirable technique for the conformal
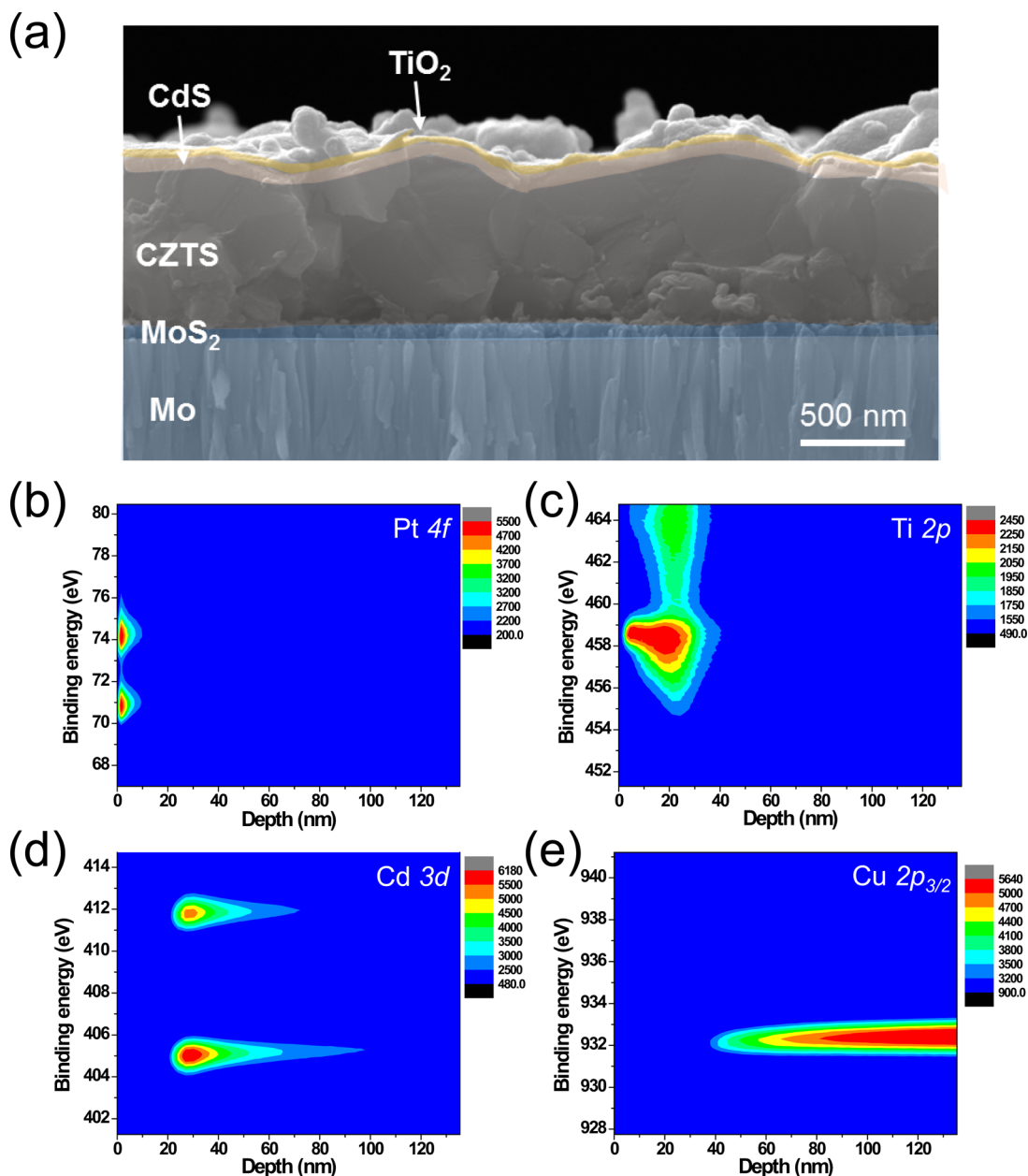
Figure 6. (a) Cross-sectional SEM image of a Pt/ALD-TiO$_2$/CdS/CZTS photocathode. (b−e) The corresponding elemental contour plots for the Pt, Ti, Cd, and Cu XPS signals.

coating of a thin layer. The thickness-dependent transmittance of ALD-TiO$_2$ layer is presented in Figure S12. As expected, the transmittance of TiO$_2$ layer decreases with the increasing thickness. We adopted 600 cycles ALD-TiO$_2$ to avoid optical loss within the visible light range (400−800 nm), which is close to the absorption range of CZTS. Figure 6a shows the cross-sectional SEM image for the Pt/ALD-TiO$_2$/CdS/CZTS electrode. Thin TiO$_2$ and CdS were observed as conformal layers covering the underneath CZTS films. To further confirm the vertical distribution of the different layers in the photoelectrode, contour plots were constructed using X-ray photoelectron spectroscopy (XPS) depth profile analysis (Figure 6b−e). XPS contour plots clearly show the sequential stacks of Pt/TiO$_2$/CdS/CZTS with distinct boundaries, implying conformal coating of the TiO$_2$ and CdS layers and no exposure of CdS and CZTS to the electrolyte. The thicknesses of TiO$_2$ and CdS were estimated to be 25 and 35

nm, respectively. The current density−potential and current density−time curves are presented in Figure 7. The ALD-TiO$_2$-deposited CZTS photocathode (Pt/ALD-TiO$_2$/CdS/CZTS) exhibited improved stability during the PEC measurement (75% retained photocurrent after 1 h) with a minor variation due to the accumulation and detachment of bubbles on the surface of the electrode adjacent to the insulating epoxy, as shown in Figure S13. Although the ALD-TiO$_2$-deposited photocathode revealed better stability than its solution-deposited counterpart, the photocurrent of the Pt/ALD-TiO$_2$/CdS/CZTS photocathode decreased continuously during the long-term stability test: only 30% of the photocurrent was maintained after 5 h (Figure S14). Paracchino et al. reported an enhanced stability of the Cu$_2$O photocathode with the protection of a double layer of ALD-TiO$_2$ and ALD-TiO$_2$-aluminum-doped ZnO, but the photocurrent of ALD-protected Cu$_2$O decreased by 50% after only 20 min.[5] They ascribed the
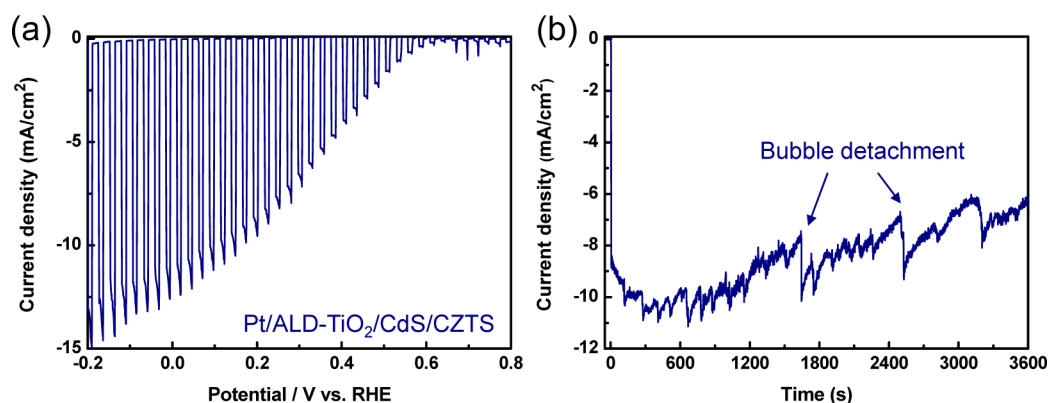
Figure 7. (a) Current density−potential curves of a Pt/ALD-TiO₂/CdS/CZTS photocathode in a phosphate-buffered aqueous solution at pH 6.85 under chopped solar-simulated light illumination (AM 1.5G) and (b) the corresponding current density−time curve with an applied bias of 0 V vs RHE.

instability to a possible reduction of TiO_2 to $Ti(OH)_3$. Rovelli et al. also observed 55% of the retaining photocurrent after 15 min for a similarly ALD-protected CZTS photocathode in the structure of ALD-TiO₂/AZO/CdS/Mo. They claimed that the photocurrent drop was due to the mass-transfer limitation and bubble formation in the electrolyte side, rather than the instability of the protection layer. This explanation was supported by the fact that the photocurrent is recovered to some extent by several means such as by depositing an additional layer of Pt catalyst, by replacing the used electrolyte with a fresh solution, and even by simple agitation of the electrolyte.[38] Similarly, we observed that the photocurrent drop of our CZTS-based photocathode was completely recovered after 12 h, indicating that the photocurrent drop could originate from the mass-transfer-related issue and bubble formation.

The amount of evolved H_2 from the Pt/ALD-TiO₂/CdS/CZTS photocathode was also evaluated. As shown in Figure 8,
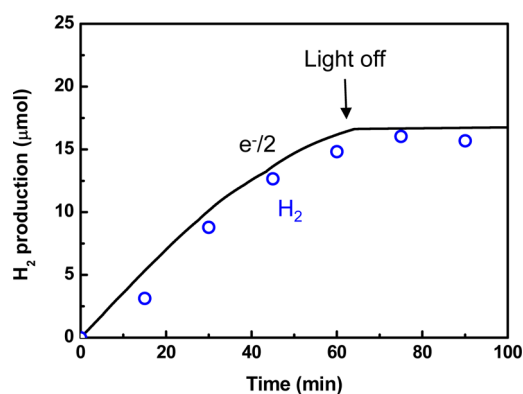

Figure 8. Time course curve of H_2 evolution over the Pt/ALD-TiO₂/CdS/CZTS photocathode under simulated sunlight (AM 1.5G) at 0 V vs RHE. The solid line denotes the time course curve for one-half of the electrons passing through the outer circuit (e^-/2).

Pt/ALD-TiO₂/CdS/CZTS photocathode revealed 90−95% of faradaic efficiency, indicating the absence of side reactions. Incident photon-to-current efficiency (IPCE) of the Pt/ALD-TIO₂/CdS/CZTS photocathode was investigated under irradiation of monochromatic light with various wavelengths at 0 V vs RHE. The photon flux was determined using a calibrated Si photodiode. The obtained IPCE spectra is shown

in Figure S15. By converting the spectra into $[h\nu \ln(1 - IPCE)]^2$ versus photon energy ($h\nu$/eV) plot, the band gap energy (E_g) of the CZTS was estimated to be 1.53 eV, which is close to the literature value.[24]

In summary, we demonstrated highly efficient photocathodes based on low-cost solution-processed CZTS thin films. To accomplish this, we developed a desirable synthetic route for homogeneous hybrid inks containing ionic Cu, Sn, and thiourea together with well-dispersed Zn nanoparticles, enabling a high-quality CZTS photocathode. Liquid Raman spectroscopy allowed us to understand the role of Sn−thiourea complexation in the preparation of the hybrid ink, which is capable of hindering the polymerization of the Cu ion−thiourea complex and in turn the undesirable segregation in the precursor ink state. The air-drying temperature of the as-deposited hybrid ink-derived CZTS films played an important role in determining the phase evolution and crystallization. High drying temperatures above 300 °C resulted in nonuniformity and elemental loss, whereas low drying temperatures near 150 °C were unable to remove carbon impurities from the precursor films. The PEC performance of our hybrid ink-derived CZTS photocathode was greatly enhanced by the adoption of thin n-type overlayers and Pt cocatalyst, particularly in the phosphate buffer solution. Despite the exceptionally high photocurrent of solution-processed TiO₂ deposited photocathode reaching 21.5 mA cm⁻², the faradaic efficiency is within a range of 45−55%, indicating the presence of a side reaction possibly due to an incomplete coverage. For better stability, an ALD-TiO₂ layer was used, and the ALD-TiO₂-deposited photocathode retained 75% of its initial photocurrent after 1 h of measurement time at 0 V vs RHE. GC was used to detect the hydrogen evolved from the CZTS-based photocathode, and the faradaic efficiency reached nearly 100%. Our hybrid ink-derived CZTS photocathodes clearly demonstrated a great potential in solar water splitting for viable hydrogen production via photoelectrochemical tandem cells.

■ ASSOCIATED CONTENT

ⓢ Supporting Information

The Supporting Information is available free of charge on the ACS Publications website at DOI: 10.1021/acsenergylett.6b00453.

Experimental section and Figures S1−S15: TG and DSC of the dried CZTS hybrid ink; Raman spectra for thiourea and the Cu−thiourea solution; relative

composition ratio of each element and carbon concentration; SEM images of a hybrid ink-derived CZTS thin film; Raman scattering spectra with 532 and 325 nm excitation wavelengths; current density−potential curves of CZTS, Pt/CZTS, and Pt/CdS/CZTS thin films; schematics of band diagram; H_2 evolution over the Pt/solution-TiO_2/CdS/CZTS; current density−potential curves of a Pt/s-TiO_2/CdS/CZTS; thickness-dependent transmittance of ALD-TiO_2 films; photographs of PEC device; stability test (5 h) by the current density−time curve; IPCE spectrum of Pt/ALT-TiO_2/CdS/CZTS photocathode (PDF)

■ AUTHOR INFORMATION

Corresponding Author

*E-mail: jmoon@yonsei.ac.kr. Tel.: +82-2-2123-2855. Fax: +82-2-312-5375.

ORCID

Jooho Moon: 0000-0002-6685-9999

Notes

The authors declare no competing financial interest.

■ ACKNOWLEDGMENTS

■ REFERENCES

(1) Miller, E. L. Photoelectrochemical Water Splitting. *Energy Environ. Sci.* **2015**, *8*, 2809−2810.

(2) Fujishima, A.; Honda, K. Electrochemical Photolysis of Water at a Semiconductor Electrode. *Nature* **1972**, *238*, 37−38.

(3) Hu, S.; Xiang, C.; Haussener, S.; Berger, A. D.; Lewis, N. S. An Analysis of the Optimal Band Gaps of Light Absorbers in Integrated Tandem Photoelectrochemical Water-splitting Systems. *Energy Environ. Sci.* **2013**, *6*, 2984−2993.

(4) Huang, Q.; Ye, Z.; Xiao, X. Recent Progress in Photocathodes for Hydrogen Evolution. *J. Mater. Chem. A* **2015**, *3*, 15824−15837.

(5) Paracchino, A.; Laporte, V.; Sivula, K.; Grätzel, M.; Thimsen, E. Highly Active Oxide Photocathode for Photoelectrochemical Water Reduction. *Nat. Mater.* **2011**, *10*, 456−461.

(6) Morales-Guio, C. G.; Tilley, S. D.; Vrubel, H.; Grätzel, M.; Hu, X. Hydrogen Evolution from a Copper(I) Oxide Photocathode Coated with an Amorphous Molybdenum Sulphide Catalyst. *Nat. Commun.* **2014**, *5*, 3059.

(7) Dias, P.; Schreier, M.; Tilley, S. D.; Luo, J.; Azevedo, J.; Andrade, L.; Bi, D.; Hagfeldt, A.; Mendes, A.; Grätzel, M.; et al. Transparent Cuprous Oxide Photocathode Enabling a Stacked Tandem Cell for Unbiased Water Splitting. *Adv. Energy Mater.* **2015**, *5*, 1501537.

(8) Li, C.; Hisatomi, T.; Watanabe, O.; Nakabayashi, M.; Shibata, N.; Domen, K.; Delaunay, J.-J. Positive Onset Potential and Stability of Cu_2O-based Photocathodes in Water Splitting by Atomic Layer Deposition of a Ga_2O_3 Buffer Layer. *Energy Environ. Sci.* **2015**, *8*, 1493−1500.

(9) Kumagai, H.; Minegishi, T.; Sato, N.; Yamada, T.; Kubota, J.; Domen, K. Efficient Solar Hydrogen Production from Neutral Electrolytes using Surface-modified $Cu(In,Ga)Se_2$ Photocathodes. *J. Mater. Chem. A* **2015**, *3*, 8300−8307.

(10) Gunawan; Septina, W.; Ikeda, S.; Harada, T.; Minegishi, T.; Domen, K.; Matsumura, M. Platinum and Indium Sulfide-modified $CuInS_2$ as Efficient Photocathodes for Photoelectrochemical Water Splitting. *Chem. Commun.* **2014**, *50*, 8941−8943.

(11) Moriya, M.; Minegishi, T.; Kumagai, H.; Katayama, M.; Kubota, J.; Domen, K. Stable Hydrogen Evolution from CdS-Modified

(12) Yokoyama, D.; Minegishi, T.; Jimbo, K.; Hisatomi, T.; Ma, G.; Katayama, M.; Kubota, J.; Katagiri, H.; Domen, K. H_2 Evolution from Water on Modified Cu_2ZnSnS_4 Photoelectrode under Solar Light. *Appl. Phys. Express* **2010**, *3*, 101202.

(13) Guijarro, N. s.; Prévot, M. S.; Sivula, K. Enhancing the Charge Separation in Nanocrystalline Cu_2ZnSnS_4 Photocathodes for Photoelectrochemical Application: the Role of Surface Modifications. *J. Phys. Chem. Lett.* **2014**, *5*, 3902−3908.

(14) Guan, Z.; Luo, W.; Zou, Z. Formation Mechanism of ZnS Impurities and Their Effect on Photoelectrochemical Properties on a Cu_2ZnSnS_4 Photocathode. *CrystEngComm* **2014**, *16*, 2929−2936.

(15) Zhang, Y.; Ouyang, S.; Yu, Q.; Li, P.; Ye, J. Modulation of Sulfur Partial Pressure in Sulfurization to Significantly Improve the Photoelectrochemical Performance over the Cu_2ZnSnS_4 Photocathode. *Chem. Commun.* **2015**, *51*, 14057−14059.

(16) Guan, Z.; Luo, W.; Xu, Y.; Tao, Q.; Wen, X.; Zou, Z. Aging Precursor Solution in High Humidity Remarkably Promoted Grain Growth in Cu_2ZnSnS_4 Films. *ACS Appl. Mater. Interfaces* **2016**, *8*, 5432−5438.

(17) Jiang, F.; Harada, T.; Kuang, Y.; Minegishi, T.; Domen, K.; Ikeda, S. Pt/In_2S_3/CdS/Cu_2ZnSnS_4 Thin Film as an Efficient and Stable Photocathode for Water Reduction under Sunlight Radiation. *J. Am. Chem. Soc.* **2015**, *137*, 13691−13697.

(18) Chaudhuri, T. K.; Tiwari, D. Earth-abundant Non-toxic Cu_2ZnSnS_4 Thin Films by Direct Liquid Coating from Metal−thiourea Precursor Solution. *Sol. Energy Mater. Sol. Cells* **2012**, *101*, 46−50.

(19) Kim, Y.; Woo, K.; Kim, I.; Cho, Y. S.; Jeong, S.; Moon, J. Highly Concentrated Synthesis of Copper-zinc-tin-sulfide Nanocrystals with Easily Decomposable Capping Molecules for Printed Photovoltaic Applications. *Nanoscale* **2013**, *5*, 10183−10188.

(20) Woo, K.; Kim, Y.; Moon, J. A Non-toxic, Solution-processed, Earth Abundant Absorbing Layer for Thin-film Solar Cells. *Energy Environ. Sci.* **2012**, *5*, 5340−5345.

(21) Todorov, T. K.; Reuter, K. B.; Mitzi, D. B. High-Efficiency Solar Cell with Earth-Abundant Liquid-Processed Absorber. *Adv. Mater.* **2010**, *22*, E156−E159.

(22) Todorov, T. K.; Tang, J.; Bag, S.; Gunawan, O.; Gokmen, T.; Zhu, Y.; Mitzi, D. B. Beyond 11% Efficiency: Characteristics of State-of-the-Art $Cu_2ZnSn(S,Se)_4$ Solar Cells. *Adv. Energy Mater.* **2013**, *3*, 34−38.

(23) Bag, S.; Gunawan, O.; Gokmen, T.; Zhu, Y.; Todorov, T. K.; Mitzi, D. B. Low Band Gap Liquid-Processed CZTSe Solar Cell with 10.1% Efficiency. *Energy Environ. Sci.* **2012**, *5*, 7060−7065.

(24) Kim, K.; Kim, I.; Oh, Y.; Lee, D.; Woo, K.; Jeong, S.; Moon, J. Influence of Precursor Type on Non-toxic Hybrid Inks for High-Efficiency Cu_2ZnSnS_4 Thin-film Solar Cells. *Green Chem.* **2014**, *16*, 4323−4332.

(25) Kumar, M.; Dubey, A.; Adhikari, N.; Venkatesan, S.; Qiao, Q. Strategic Review of Secondary Phases, Defects and Defect-Complexes in Kesterite CZTS−Se Solar Cells. *Energy Environ. Sci.* **2015**, *8*, 3134−3159.

(26) Xin, H.; Katahara, J. K.; Braly, I. L.; Hillhouse, H. W. 8% Efficient $Cu_2ZnSn(S,Se)_4$ Solar Cells from Redox Equilibrated Simple Precursors in DMSO. *Adv. Energy Mater.* **2014**, *4*, 1301823.

(27) Kannan, V.; Rajesh, N.; Ganesh, R. B.; Ramasamy, P. Growth and Characterization of Bisthiourea-Zinc Acetate, a New Nonlinear Optical Material. *J. Cryst. Growth* **2004**, *269*, 565−569.

(28) Selvakumar, S.; Kumar, S. R.; Joseph, G. P.; Rajarajan, K.; Madhavan, J.; Rajasekar, S.; Sagayaraj, P. Growth and Characterization of Pure and Doped Bis(thiourea) Cadmium Acetate Single Crystals. *Mater. Chem. Phys.* **2007**, *103*, 153−157.

(29) Kumari, R. G.; Ramakrishnan, V.; Carolin, M. L.; Kumar, J.; Sarua, A.; Kuball, M. Raman Spectral Investigation of Thiourea Complexes. *Spectrochim. Acta, Part A* **2009**, *73*, 263−267.

(30) Granqvist, C. G. *Handbook of Inorganic Electrochromic Materials*; Elsevier Science: Amsterdam, Netherlands, 1995.

CuGaSe$_2$ Photoelectrode under Visible-Light Irradiation. *J. Am. Chem. Soc.* **2013**, *135*, 3733−3735.

(31) Kim, J.; Yang, W.; Oh, Y.; Kim, J.; Moon, J. Template-directed Fabrication of Vertically Aligned Cu_2ZnSnS_4 Nanorod Arrays for Photoelectrochemical Applications via a Non-toxic Solution Process. *J. Alloys Compd.* **2017**, *691*, 457−465.

(32) Fontané, X.; Calvo-Barrio, L.; Izquierdo-Roca, V.; Saucedo, E.; Pérez-Rodriguez, A.; Morante, J.; Berg, D.; Dale, P.; Siebentritt, S. In-depth Resolved Raman Scattering Analysis for the Identification of Secondary Phases: Characterization of Cu_2ZnSnS_4 Layers for Solar Cell Applications. *Appl. Phys. Lett.* **2011**, *98*, 181905.

(33) Chen, S.; Walsh, A.; Gong, X. G.; Wei, S. H. Classification of Lattice Defects in the Kesterite Cu_2ZnSnS_4 and $Cu_2ZnSnSe_4$ Earth-Abundant Solar Cell Absorbers. *Adv. Mater.* **2013**, *25*, 1522−1539.

(34) Berg, D. M.; Arasimowicz, M.; Djemour, R.; Gütay, L.; Siebentritt, S.; Schorr, S.; Fontané, X.; Izquierdo-Roca, V.; Pérez-Rodriguez, A.; Dale, P. J. Discrimination and Detection Limits of Secondary Phases in Cu_2ZnSnS_4 Using X-ray Diffraction and Raman Spectroscopy. *Thin Solid Films* **2014**, *569*, 113−123.

(35) Guijarro, N.; Prévot, M. S.; Yu, X.; Jeanbourquin, X. A.; Bornoz, P.; Bourée, W.; Johnson, M.; Le Formal, F.; Sivula, K. A Bottom-Up Approach toward All-Solution-Processed High-Effi ciency Cu(In,Ga)-S_2 Photocathodes for Solar Water Splitting. *Adv. Energy Mater.* **2016**, *6*, 1501949.

(36) Sivula, K.; van de Krol, R. Semiconducting Materials for Photoelectrochemical Energy Conversion. *Nat. Rev. Mater.* **2016**, *1*, 15010.

(37) Zhang, L.; Minegishi, T.; Kubota, J.; Domen, K. Hydrogen Evolution from Water using $Ag_xCu_{1-x}GaSe_2$ Photocathodes under Visible Light. *Phys. Chem. Chem. Phys.* **2014**, *16*, 6167−6174.

(38) Rovelli, L.; Tilley, S. D.; Sivula, K. Optimization and Stabilization of Electrodeposited Cu_2ZnSnS_4 Photocathodes for Solar Water Reduction. *ACS Appl. Mater. Interfaces* **2013**, *5*, 8018−8024.

(39) Huang, S.; Luo, W.; Zou, Z. Band Positions and Photo-electrochemical Properties of Cu_2ZnSnS_4 Thin Films by the Ultrasonic Spray Pyrolysis Method. *J. Phys. D: Appl. Phys.* **2013**, *46*, 235108.

(40) Auinger, M.; Katsounaros, I.; Meier, J. C.; Klemm, S. O.; Biedermann, P. U.; Topalov, A. A.; Rohwerder, M.; Mayrhofer, K. J. J. Near-Surface Ion Distribution and Buffer Effects During Electro-chemical Reactions. *Phys. Chem. Chem. Phys.* **2011**, *13*, 16384−16394.